Progress in Nuclear Energy 116 (2019) 148–157

Contents lists available at ScienceDirect

Progress in Nuclear Energy

journal homepage: www.elsevier.com/locate/pnucene

Aerosol depositional characteristics in piping assembly under varying flow conditions

A.K. Dwivedi[a], Arshad Khan[c], S.N. Tripathi[a,*], Manish Joshi[c], Gaurav Mishra[b], Dinesh Nath[a], Naveen Tiwari[d], B.K. Sapra[c]

[a] Department of Civil Engineering, IIT, Kanpur, 208 016, India
[b] Nuclear Engineering and Technology Programme, Mechanical Engineering Department, IIT, Kanpur, 208 016, India
[c] Radiological Physics and Advisory Division, Bhabha Atomic Research Centre, Mumbai, 400 085, India
[d] Department of Chemical Engineering, IIT, Kanpur, 208016, India

ARTICLE INFO

Keywords:
Aerosol
Deposition
Coagulation
Modeling
CFD
Population balance model

ABSTRACT

In the event of a nuclear reactor accident, large amount of radioactivity in the form of fission products may get released to the piping assembly of primary heat transport system. These fission products mostly in the form of aerosol particles get deposited on the inner surface of the piping system due to various depositional processes. The removal processes in the complex piping system are controlled to a large extent by the thermal-hydraulic conditions like temperature, pressure and flow rates. These parameters generally vary with time and therefore must be carefully monitored to predict the aerosol behavior in the piping system. Experimental determination of the deposition fraction, interpretation of the role of controlling parameters and development/validation of theoretical models are key areas gaining constant attention among researchers. In the present work, experiments were conducted in a piping assembly consisting of bends and horizontal-vertical orientation at two different carrier gas flow rates. Deposition fractions in the test assembly were estimated and the role of different dynamical processes (thermophoresis, gravitation and bend impaction) was interpreted. The computational fluid dynamics modeling approach is used for theoretical simulation in this work. Aerosol behavior in terms of number concentration, particle size distribution, and particle deposition in the piping system was simulated with the computational fluid dynamics software ANSYS Fluent 16.0 and the results were compared with experimental measurements (wherever applicable).

1. Introduction

In a nuclear reactor, the most commonly postulated accident scenario is a core meltdown accident resulting to the release of radioactive material in the form of aerosols into the primary heat transport system and subsequently into the containment. Aerosol concentrations in a reactor accidents situation can typically be as high as 100 g/m^3, and the corresponding number density can exceed $10^{13}/m^3$ (Sher et al., 1994). The removal process of aerosol depends on the size of particles that determines how many particles get deposit or traval across the orientation and reach to the other end of the piping system. The released aerosol particles typically have a range of sizes varying from 0.1 μm to 10 μm (Williams, 1990). Study of the number of core damage experiments concludes that the best estimate of number size distribution parameters are: $d_g = 0.44\,\mu$m and $\sigma_g = 1.81$, where d_g is the geometric mean diameter, and σ_g is the geometric standard deviation (Sher and Hobbins, 2011). The salient features of aerosol physics that affect the behavior of the aerosols under reactor accident conditions are their nucleation, growth, shape, deposition on surfaces, and re-suspension. The nucleation of particles under high supersaturation conditions is the predominant source of formation of aerosols in reactor accidents. The formed aerosol particles grow by continued condensation of vapor on these nucleated particles and further grow by coagulation processes. Growth of these aerosols can also be governed by their hygroscopic properties (Mishra et al., 2019). In a quasi-steady state environment with no continuous source of aerosol, an aerosol subjected to particle growth by coagulation and gravitational deposition onto surface develops a size distribution that is well approximated by a log-normal distribution. Whereas, when there is a continuous source of aerosol or when there are complex processes involving engineered safety features much more complicated size distributions develop. The released aerosol gets deposited onto the inner surface of the piping system by various

* Corresponding author.
E-mail address: snt@iitk.ac.in (S.N. Tripathi).

https://doi.org/10.1016/j.pnucene.2019.04.007
Received 2 November 2018; Received in revised form 23 March 2019; Accepted 12 April 2019

mechanisms like gravitational settling, Brownian diffusion, thermophoretic deposition, and by other deposition mechanisms (Maruyama et al., 1999a; Le Marois and Megnin, 1994; Modi et al., 2014). To quantify the correct estimate of deposition, the identification and understanding of the aforementioned deposition mechanisms are of great importance. These mechanisms are significantly affected by different flow and thermodynamic conditions.

(Liu and Agarwal, 1974) have performed aerosol deposition studies on particles ranging in size from 1.4 to 21 μm in vertical turbulent pipe-flow. They found the predominant mechanism to be an inertial effect resulting from the particle mass being acted on by the fluid turbulence. Thermophoresis also plays a significant role in particle deposition. Considerable work has been done in the past to study thermophoretic particle deposition under laminar and turbulent flow conditions. (Shimada et al., 1994), and (Stratmann and Fissan, 1989) performed experimental studies with particle sizes (380 nm down to below 20 nm) and found good agreement of experimental data with theoretical models using a thermophoretic coefficient expression of (Talbot et al., 1980). Theoretical studies on thermophoresis include the work done by (Walker et al., 1979) and (Batchelor and Shen, 1985). (Maruyama et al., 1999b) have performed a series of aerosol deposition experiments to investigate the deposition of fission product vapor and aerosols onto the inner surface of the reactor coolant piping system during a reactor accident. They found that the local thermo-fluid dynamic conditions highly influence, CsI deposition profile due to vapor condensation and thermophoretic aerosol deposition. The aerosol deposition experiments in the piping assembly to investigate the dry deposition of metal aerosols were conducted by (Modi et al., 2014). The experimental results were then compared with predictions made from SOPHEROS model of computer code ASTEC (Accident Source Term Evaluation Code) and found to be within 8% of those estimated by the code. In their study, thermophoresis was found to be major deposition mechanism with gravitational settling predominant in pipe sections with low thermal gradients.

The modeling of aerosol transport processes needs a coupling of the aerosol dynamic and thermal hydraulic models. In most of the reactor containment codes developed so far (ASTEC, COCOSYS, CONTAIN, MELCOR, SPACE), all these interrelation processes are modeled (Šadek et al., 2017; Bae et al., 2018). There are several experimental programs (VICTORIA, VANAM, and DEMONA) aimed at the validation of these codes in which extensive studies on the aerosol transport and deposition in containment geometries (Jokiniemi et al., 1998) are performed. Among these the VANAM tests were the most comprehensive one. The VANAM tests demonstrated the need for multi-compartment accident analyses (Firnhaber et al., 1996) to study the depositional phenomena. In the STORM experiment, the pipe (5 m long) is streamed by tin oxide (SnO_2) aerosol with nitrogen and steam as a carrier gas. In this experiment, the deposit was formed mainly by thermophoresis, which resulted in a much denser and stronger particle layer. It was found that the poly-disperse aerosol form a stronger deposit with lower porosity than mono-disperse particles.

(Longest and Xi, 2007) simulated the transport and deposition of fine aerosol particles in a duct with an elbow using the commercial CFD software FLUENT. The particles were released from a capillary at the inlet of the duct, and carried through the duct by air flow. They found that a direct Lagrangian transport model with appropriate user-defined routine provides an effective approach for predicting the deposition of nanoparticles (Parker et al., 2008). carried out CFD simulation of aerosol deposition in vertical pipe flow for steady-state (time-averaged stationery) condition using Lagrangian particle tracking approach. In their study, they found that the CFD-simulated aerosol deposition was highly dependent on the choice of turbulent model, wall treatment and mesh resolution.

In the present study, experiments were performed in the piping system of the National Aerosol Test Facility (NATF), Bhabha Atomic Research Center (BARC), Mumbai, India using metal aerosols (zinc) in dry environments to measure and interpret aerosol mass concentration, mass size distribution and deposition fraction. The role of different removal mechanisms towards the spatial mass characteristics and depositional patterns has also been discussed. These experiments were performed at two different carrier gas flow rates. The commercial CFD software FLUENT is used to determine the distribution of temperature, velocity, pressure, and turbulence quantities in the piping system. In addition to the in-built models for turbulence, heat transfer and flow in the commercial CFD code (FLUENT), a new sub-model PBM (population balance model) is used to describe the coagulation process and to compute the number concentration along with the size distribution at different sections of the piping. In the sub-model, coagulation kernels are incorporated through user-defined function (UDF). For gravitational deposition, we have used Crump and Seinfeld (1981) model and fan model (Shimada et al., 1989) The experimental results are compared with the CFD modeled results.

2. Experimental details

2.1. Experimental setup

The experiments were performed in the NATF facility which is a medium-scale facility for carrying out aerosol behavior experiments under simulated nuclear accident conditions. The experimental set-up is mainly comprised of a Plasma Torch Aerosol Generator, piping system, carrier gas delivery system, a powder feeder, and a plenum chamber. The plenum chamber is a double walled water-cooled stainless steel chamber of volume $0.04\ m^3$ (length $0.6\ m$, and diameter $0.3\ m$) providing essential nucleation conditions for hot vapors generated from plasma zone. Water cooling system connected to the plenum chamber allows the precise control of the aerosol-laden gas temperature and creates a thermophoretic gradient. The powder feeder (model: MEC PF-3350), operating on the volumetric feed principle, is fitted with the special type of rotating disc having fine openings. Rotation of the wheel forces the powder into the exit port through the powder hose towards the plasma torch in a carefully calibrated manner. The experiment setup is schematically shown in Fig. 1. The details on the design and characterization of the plasma torch are discussed elsewhere (Sreekumar, 1996). The experiments are performed at atmospheric pressure while temperature conditions are maintained as per the test requirement. The outer surface of the piping system is exposed to the room temperature, allowing it to exchange heat with the surrounding. The total length of the piping system is $3\ m$ consisting of six straight sections, and three 90^o angle bends all having an inner diameter of $124\ mm$. The piping sections are provided with multiple ports for inserting the thermocouples and for extracting the air samples. For the measurement of the carrier gas and wall temperature, 16 numbers of factory-calibrated K-type thermocouples at different points in the piping assembly are used, and the data is recorded through data logger. In the experimental setup, eight number of thermocouples are placed inside the piping system, to monitor centerline bulk gas temperature (T_g) and remaining eight number of thermocouples are placed at different locations of the inner wall to measure corresponding wall temperatures (T_w). A $47\ mm$ filter holder made of stainless steel is used to measure the gross mass concentration (without size separation). A cascade impactor (model: PPASS-01) having 11 stages is used for the measurement of aerosol mass size distribution (Singh et al., 2005). This 11 cascade impactor has seven stages operating at normal pressure and four at low pressure (150 mm Hg). PPASS-01 works on the principal of inertial impaction and separates particles according to their aerodynamic diameter range 0.1 - 20 μm with 10 $Lmin^{-1}$ operating flow rate.

2.2. Experimental procedure

Experiments were performed at two different carrier gas flow rates to investigate the deposition behavior of metal aerosol particle in the

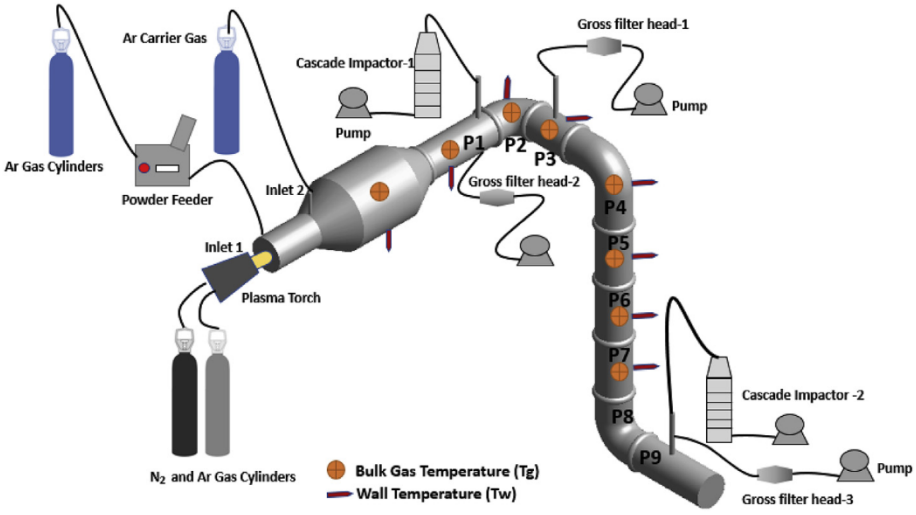

Fig. 1. Experimental setup.

piping system. At the start of each experiment, entire test assembly was cleaned with a wet cloth to minimize the total background deposition. The plasma torch was operated at 15 kW power. The Zinc oxide (ZnO) aerosol particles were generated by vaporizing Zinc (Zn) Powder using the plasma torch. Pre-weighted Zn metal powder of size $40\ \mu m$ was fed into the powder feeder which was then injected into the plasma torch at optimized feeding rate. As the exit nozzle of the powder feeder was oriented perpendicular to the plasma axis, powder falls directly on the plasma flame. The evaporated material was then transported through inlet 1 to the plenum chamber where it nucleates and forms aerosol particles. The above-described method (evaporation-condensation) offers high aerosol generation rates, and simulates the aerosol formation during the core meltdown accident. The metal powder was injected into the flame at different feed rates 1-3 g/min in various sets of experiments. The plenum chamber had an annular duct from which additional carrier gas (100 and 150 $Lmin^{-1}$) was injected which helps in mixing and transporting the formed aerosol particles. The measurements were started soon after the plasma torch was fired. During the experiment, aerosol sampling (via ports in pipe section 1,3 and 9) was carried out at regular intervals using the gross filter paper sampler for the estimation of the total mass concentration. The total sampling time for the measurements at each sampling site was two minute. Additionally, cascade impactors were employed in first and last pipe section (1 and 9) measuring the mass size distribution of traversing aerosol particles.

Filters were weighed by a gravimetric balance (model: M3P-000V001, Sartorius) under controlled temperature and humidity conditions before and after sampling. The experiments with carrier gas flow rate 100 $Lmin^{-1}$ (EXP-I) were performed with two powder feeding rates, 1 g/min (EXP-Ia) and 3 g/min (EXP-Ib). Experiments with higher flow i.e. 150 $Lmin^{-1}$ were carried out at powder feeding rate of 1 g/min. At the end of each experiment, the plasma torch was turned off, and the piping sections were then left for cooling. Once the system cools down the test sections were disassembled, and the deposited particles on the inside surface of the piping section were scraped carefully using a fine brush. The collected powder samples were then analyzed using Scanning electron microscopy (SEM) and X-ray diffraction analysis (XRD) for particle morphology and composition. X-ray diffraction is used to determine the crystalline phases and their approximate proportions present in the powder material, by examining the respective diffraction patterns. The diffraction peaks in the X-ray diffraction pattern are unique for different compounds. A copper-K_α source ($40\ kV$, $40\ mA$) and a Lynx Eye 1D detector with a discrimination voltage range of $0.18 - 0.25\ V$ were used in the current study. The surface morphology and topology of particles together with their elemental composition were determined using a Scanning Electron Microscope (SEM: ZEISS EVO MA-10) equipped with an energy dispersive spectrometer (EDS: Oxford Link ISIS300) available at IIT Kanpur.

3. Model and governing equations

The CFD approach consists of solving the continuity, momentum and energy equations in each cell of a discretized computational domain. The mass conservation equation, or continuity equation, can be written as follows:

$$\frac{\partial \rho}{\partial t} + \nabla\cdot(\rho \boldsymbol{u}) = S_m, \tag{1}$$

where ρ is the fluid density, u is the fluid velocity vector and S_m the source term. Conservation of momentum is described by

$$\frac{\partial \rho \boldsymbol{u}}{\partial t} + \nabla\cdot(\rho \boldsymbol{u}\boldsymbol{u}) = -\nabla P + -\nabla\tau + \rho \boldsymbol{g} + \boldsymbol{F}, \tag{2}$$

where P is the static pressure, τ is the stress tensor, g represents the gravitational acceleration and F is the external body force. The energy equation is given as follows:

$$\rho C_p\left[\frac{\partial T}{\partial t} + (T\boldsymbol{u})\right] = \nabla\cdot(k\nabla T) + \tau\colon \nabla \boldsymbol{u} \tag{3}$$

where C_p, T,and k are specific heat, temperature and thermal conductivity respectively.

An aerosol dynamics model is used to simulate the effect of dynamical processes on particles within a homogeneous control volume. A CFD model describes the effect of transport processes across the boundaries of control volumes on the particles. The Population Balance Model (PBM) is a particle-dynamics model coupled with FLUENT, permits simulation of the formation, transformation (i.e., growth, shrinkage, and coagulation) and transport of particles in gases and liquids. Aerosol particle transport and dynamics is represented mathematically by a population balance equation, usually referred to as the general dynamic equation (Gelbard and Seinfeld, 1979).

3.1. Particle coagulation

Assuming that $n(V)$ is the concentration of particles having volume V, the population balance equation can be written as

$$\frac{\partial n(V,t)}{\partial t} + \nabla\cdot \boldsymbol{v} n(V,t) = B_A - D_A, \tag{4}$$

where B_A and D_A are the birth and death rates due to coagulation, respectively. The equation below represents the rate of birth of particles $n(V, t)$ of volume V at any time t by the collisions between particles of volumes $\bar{V}$ and $V - \bar{V}$.

$$B_A = \frac{1}{2}\int_0^V \beta_{V-\bar{V},\bar{V}}\, n(V-\bar{V}, t)n(\bar{V}, t)d\bar{V}. \tag{5}$$

The term 1/2 prevents counting the collisions twice, once each for the two colliding particles and $\beta_{V-\bar{V},\bar{V}}$ denotes the coagulation kernal. The death rate D_A of particles of diameter V due to coagulation is defined as follows:

$$D_A = n(V, t)\int_0^\infty \beta_{V-\bar{V},\bar{V}}\, n(\bar{V}, t)d\bar{V}. \tag{6}$$

In this work, an Eulerian-Eulerian approach is used to model the particle-laden flow in the piping section. This was further accomplished by the mixture model, which is a simplified multiphase model. In PBM we have used the discrete method, which allows the direct tracking of the local particle size distribution (PSD). The collision frequency function is computed using the Fuchs interpolation formula and implement in FLUENT through UDF. Similarly, we have implemented the Brownian, gravitational, turbulent shear and turbulent inertia coagulation kernels, as described in (Seinfeld and Pandis, 1998), through UDF.

$$\beta = \beta_{Brow.} + \beta_{grav.} + \beta_{turb.\ shear} + \beta_{turb.\ iner.} \tag{7}$$

In the above equation the coagulation kernel due to Brownian motion is given by:

$$\beta_{Brow.} = 2\pi(D_1 + D_2)(d_1 + d_2)\left[\frac{(d_1+d_2)}{d_1+d_2+2\sqrt{g_1^2+g_2^2}} + \frac{8(D_1+D_2)}{(d_1+d_2)\sqrt{c_1^2+c_2^2}}\right]^{-1} \tag{8}$$

where d_i and D_i are the diameter and Brownian diffusivities corresponding to the two coagulating particles represented by the index i. The variables D_i, g_i and c_i are given as below:

$$D_i = \frac{KTC_c}{3.0\pi\mu d_i}, \quad g_i = \frac{1.0}{3.0 d_i l_i}[(d_i + l_i)^3 - (d_i^2 + l_i^2)^{3/2}] - d_i, \quad c_i = \sqrt{\frac{8.0KT}{\pi m_i}},$$

where mass of the particles, m_i, the Cunningham's slip factor, C_c, and l_i are written as below:

$$m_i = \frac{\pi}{6}d_i^3\rho, \quad C_c = 1.0 + \frac{2.0\lambda}{d_i}\left[1.257 + 0.4 \times 2.718^{(-1.1 d_i/2\lambda)}\right], \quad l_i = \frac{8.0D_i}{\pi c_i},$$

Where K, μ and λ are Boltzman's constant, dynamic viscosity and mean free path of the gas respectively. When particles are subjected to some external force (gravitational force) they will have a preferred direction of motion superimposed on their random motions. To account this effect a gravitational kernel is added in the coagulation and is given by the following equation:

$$\beta_{grav.} = \frac{\pi}{4}(d_1 + d_2)^2||v_{t1} - v_{t2}||E \tag{9}$$

The terminal velocity, vt_i, and the efficiency factor of collisions, E, in above equation (Eq. (9)) are given as below:

$$v_{t_l} = \begin{cases} \frac{1}{18\mu}d_i^2\rho C_c g; & if \quad J_1 < 2 \\ \frac{\mu}{\rho d_l} exp(-3.070 + 0.9935J_1 - 0.0178J_1^2); & if \quad J_1 > d_2 \end{cases} \tag{10}$$

where,

$$J_1 = log\left(\frac{4d_2^3\rho_g\rho_p g C_c}{3\mu^2}\right),$$

$$E = \begin{cases} \frac{1}{2}\left(\frac{d_2}{d_1+d_2}\right)^2; & if \quad d_2 < d_1, \\ \frac{1}{2}\left(\frac{d_1}{d_1+d_2}\right)^2; & if \quad d_1 < d_2, \end{cases} \tag{11}$$

The other minor mechanisms that may effect the coagulation include the turbulent shear and turbulent inertia. These are mostly localized near the walls and the inner surfaces of the chamber. The aggregation kernel due to turbulent shear and turbulent inertia are given as below:

$$\beta_{turb.\ shear} = \sqrt{\frac{8\pi\varepsilon}{15\mu}}\left(\frac{d_1}{2} + \frac{d_2}{2}\right)^3 \tag{12}$$

$$\beta_{turb.\ iner.} = \pi\frac{\varepsilon^{0.75}}{g\mu^{0.25}}\left(\frac{d_1}{2} + \frac{d_2}{2}\right)^2||v_{t_1} - v_{t_2}|| \tag{13}$$

where ε is the turbulent kinetic energy dissipation rate and μ is dynamic viscosity.

3.2. Particle deposition

The principal processes governing the removal of aerosol particles inside the piping system are gravitational settling, diffusiophoretic and thermophoretic deposition onto the surface. Aerosol particles adhere to the wall surface on collision, creating a concentration gradient which further leads to the diffusion of aerosol particles towards the surface. The diffusional flux can be described by a modified form of Fick's law (Ghosh et al., 2017; Sapra et al., 2008)

$$J = -(\varepsilon_p + D)\frac{\partial n}{\partial y} - \hat{\imath}u_{set}n \tag{14}$$

where n is the particle number concentration, D is the Brownian diffusivity of the particles, ε_p is the turbulent (eddy) diffusivity of the particle, $\hat{\imath}$ denotes the orientation of the surface and u_{set} is the settling velocity of the particle.

The flux is further modified by adding an extra term for the thermophoretic effect (u_{th}) in Eq. (14)

$$J = -(\varepsilon_p + D)\frac{\partial n}{\partial y} - \hat{\imath}u_{set}n + u_{th}n, \tag{15}$$

The solution of Eq. (15) follows from the detailed derivation of the Crump-Seinfeld model and one can obtain the solution with combined effect of gravitational settling and thermophoresis for floor and ceiling (Ghosh et al., 2017):

$$u_{top} = \frac{u^* - u_{set} + u_{th}}{1 + \frac{u^*}{u_{th} - u_{set}}\left(1 - \exp\left(-\delta(\frac{u_{th} - v_{set}}{D})cot^{-1}(\frac{d_s}{\delta})\right)\right]}, \tag{16}$$

$$u_{floor} = \frac{u^* + u_{set} + u_{th}}{1 + \frac{u^*}{u_{th} + u_{set}}\left(1 - \exp\left(-\delta(\frac{u_{th} + v_{set}}{D})cot^{-1}(\frac{d_s}{\delta})\right)\right]}. \tag{17}$$

In the above equations,

$$\delta = \sqrt{\frac{D_i}{k_e}}, \; k_e = 0.4\sqrt{\frac{2\varepsilon}{15\nu}}, \; d_s = \frac{2u^*\rho_p r^2 C_c}{9\mu}, \; u^* = \sqrt{\frac{\tau}{\rho}} \tag{18}$$

where, D_i, ε, ν, d_s and u^* are diffusion coefficient of particles, turbulent energy dissipation rate, kinematic viscosity, stopping distance of the particle and friction velocity respectively.

The settling velocity is described by the well known Stokes-Cunningham law, applies to spherical particles.

$$u_{set} = \frac{2gC_c}{9\mu\chi}(\rho_p - \rho_g)r_p^2, \tag{19}$$

where r_p, ρ_p, ρ_g, μ, χ, are the radius of particle, density of particles, density of gas, dynamic viscosity of gas, and shape factor, respectively.

When a temperature gradient is established in a gas, an aerosol particle experiences a force in the direction of decreasing temperature. The velocity of the particles due to thermophoresis is given by (Waldmann and Schmitt, 1966):

$$u_{th} = \frac{0.55\mu\nabla T}{\rho_g T} \quad for \quad d < \lambda. \tag{20}$$

When the size of particle, d, is greater than the mean free path, λ, a temperature gradient is established in the particle and this gradient affects the temperature gradient in the gas immediately surrounding the particle.

$$u_{th} = \frac{-3\mu C_c H\nabla T}{2\rho_g T} \quad for \quad d > \lambda, \tag{21}$$

where molecular accommodation cofficient, H, takes into account the effect of the temperature gradient inside the particle. The equation of H suggested by (Brock, 1962) is given below:

$$H = \left(\frac{1}{1 + 6\frac{\lambda}{d}}\right)\left(\frac{\frac{K_a}{K_p} + 4.4\frac{\lambda}{d}}{1 + 2\frac{K_a}{K_P} + 8.8\frac{\lambda}{d}}\right), \tag{22}$$

where K_a and K_p are the thermal conductivity of the air and particle.

Overall loss rate coefficient, λ_{set}, is calculated as below, where $V_{section}$ is the volume of the pipe section and A is the surface area.

$$\lambda_{set} = \frac{u_{top}A_{top} + u_{floor}A_{floor}}{V_{section}}. \tag{23}$$

λ_{set} as calculated from Eq. (23) can be incorporated in Eq. (24) (Vohra et al., 2017) for estimating the particle number concentration $N(V, t)$ as a function of time.

$$N(V, t) = \frac{n(V, t)}{1 + \lambda_{set}t}. \tag{24}$$

where t is run time of the experiment.

4. Results and discussion

The geometry of the 3D physical model is created in ANSYS design modular (ANSYS Inc., U.S.A) and meshing is done using ANSYS meshing tool (Fig. 2) A hexahedral mesh with 3.09×10^5 elements is generated. While generating the mesh, special care was taken that the cell sizes do not vary too rapidly in space, particularly in the dynamically important regions. The CFD-PBM coupled model is then solved using FLUENT 16.0 in the double precision mode to reduce roundoff errors in calculation. The SIMPLEC scheme is employed to describe pressure-velocity coupling. The time step is taken as $10^{-3}\,s$ with a maximum of 20 iterations per time step. Simulations were performed for 15 min. Various numerical residuals were monitored; these values were determined by ANSYS Fluent 16.0 from the conservation equations for mass, energy, and momentum. Convergence was determined to be achieved when the residuals for velocity and energy were less than 10^{-6} and 10^{-7} respectively.

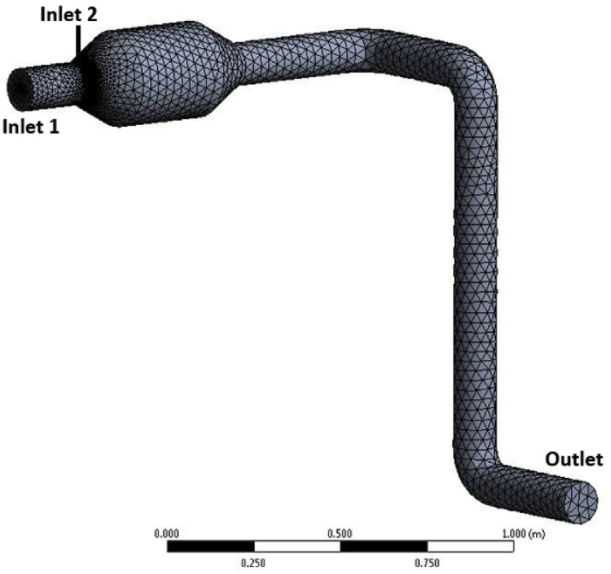

Fig. 2. Non-uniform mesh created in FLUENT meshing tool.

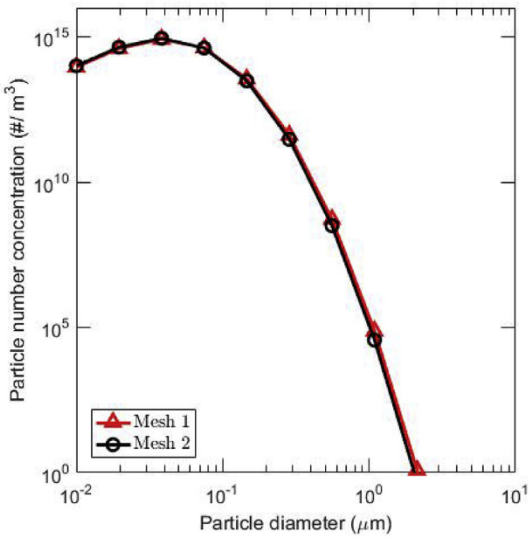

Fig. 3. Particle size distribution computed at pipe section 2 for two different mesh sizes.

Two different sizes of mesh having the number of cells 354176 and 309245 are taken for the grid sensitivity test. The particle size distribution computed at the center of pipe section after steady state have been achieved for the above two meshes. The PSD match well to each other as can be seen in Fig. 3. The simulation results reported later in this work are corresponding to the mesh having the number of cells 309245. The coagulation kernels are hooked to the model using the User Defined Function. To improve the computing efficiency, a Linux based HPC Server (128 GB of RAM per node 901 × 20, each core clock frequency 2.5 GHz) of IIT Kanpur is used to perform the simulation.

4.1. Boundary conditions

The PBE (population balance equation) was solved by the discrete method for which the bin size is determined based on the SEM and impactor data collected from the experiment. The particles size is discretized into 11 bins with size range $(0.01 - 8\,\mu m)$ with ratio exponent $q = 2.9$, where $d_{i+1}/d_i = 2^{(q/3)}$ and i refers to the bin class. The following boundary conditions have been used; the inlets are specified as a velocity inlet, and the outlet of the pipe is specified as a pressure outlet.

The choice of temperature at inlet 1 is based on the value given in (Joshi et al., 1990). The other parameters are shown in Table 1. As the nucleation process is not modeled in the present study, a constant nanoparticle (10 nm) source term is included in the modeling. This critical size of the injected aerosol has been obtained using the classical nucleation theory considering the temperature profile and the feeding rate of the powder into the piping system. Initially, the whole domain is filled with argon at temperature $293\,K$. The velocity profile of the carrier gas simulated in ANSYS FLUENT is shown in Fig. 4. The carrier gas imparts momentum to the injected aerosols and makes them travel along the piping section. The high-velocity jets coming out from the

Table 1
Parameters used for experiment.

Parameters	Velocity (m/s)	Species	T (*K*)	Volume fraction
Inlet 1	3.8	(Ar, Zn particles)	2300	Ar = 1 Zn particles = 10^{-5} size = 0.01 μm
Inlet 2	31.0	Ar	293	Ar = 1 Zn particles = 0
Walls	no-slip	–	heat loss	–

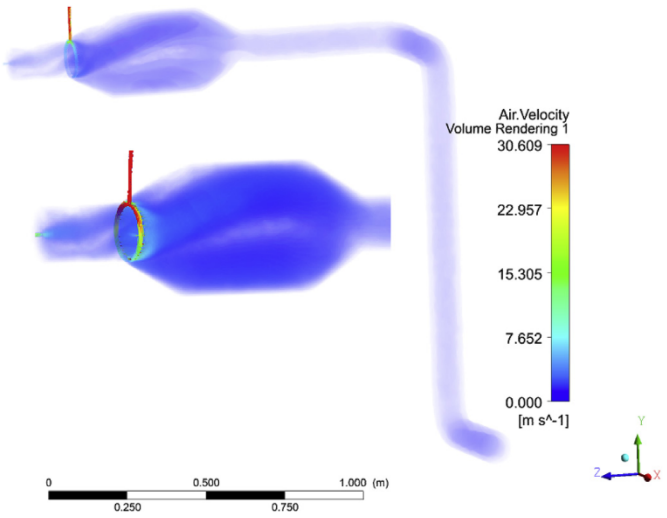

Fig. 4. A typical velocity profile of carrier gas in the piping assembly.

fine holes in the front side of the header can be seen in the zoomed figure (Fig. 4).

Table 2 shows the operating thermal hydraulic conditions such as feed rates of metal powder, plasma torch power, carrier gas, runtime, the mass of powder aersolized, etc. for the experiment presented in this work. The model parameters and constants used in the simulation are shown in Table 3.

4.2. Deposition of zinc oxide particles

The quantity of Zinc oxide deposited on the inner surface of individual sections of the plenum chamber, and piping sections are shown in Table 4 and Table 5, respectively. It can be seen a huge amount of ZnO deposition is observed near the inlet of the plenum chamber (where the plasma torch is fitted). Since the plenum chamber has 3 sections (diverging, horizontal, converging) of different lengths, so the mass deposited in different sections is normalized with their respective lengths. These normalized quantities are shown in parenthesis in Table 4. It can be calculated from the table that in 100 $Lmin^{-1}$ experiment (Exp-Ia), out of 35.38 % of total percent mass deposited in the piping system, 31.18 % deposits in the plenum chamber itself and remaining 4.2 % deposits in the pipe sections. Similarly, in Exp-II experiment, total percentage mass deposited in the piping system is 43.4 %, out of which 41.6 % deposits in plenum chamber, and 1.84 % in piping sections.

Table 2
Parameters used for Zn metal aerosol deposition experiment.

Boundary	Exp-I(a)	Exp-I(b)	Exp-II
Power of Torch (KW)	15	15	15
Run Time (min)	20	26	10
Total weight of powder aerosolized (g)	22.2	71.9	11
Total flow rate of carrier gas ($Lmin^{-1}$)	100	100	150

Table 3
Parameters used for model simulation.

Parameter	Parameter value
Density of argon ρ_g	1.44 kg/m^3
Gravitational acceleration g	9.8 m/s^2
Specific heat of argon C_P	520 J/kg-K
Thermal conductivity of argon K_a	0.01 W/m-K
Thermal conductivity of Zinc K_p	50W/m-K
Boltzman's constant K	$1.38e^{-}23m^2kg/s^{-2} - K$
Viscosity of argon μ	$3.7e^{-5}Kg/m$-s
shape factor χ	1

Table 4
Total amount of Zinc oxide deposited (in g) on the inner sections of the plenum chamber. The quantity in parenthesis are the mass deposited per unit length (in g/cm). The lengths Near Plasma, Diverging, Horizontal, and Converging sections are: 15 cm, 16.4 cm, 30.0 cm.16.4 cm

Exp.	Near Plasma	Diverging	Horizontal	Converging
Exp-I(a)	4.2722 (0.28)	1.062 (0.06)	1.696 (0.05)	0.7259 (0.04)
Exp-I(b)	8.9474 (0.59)	3.5872 (0.21)	7.2971 (0.24)	2.6048 (0.15)
Exp-II	2.7981 (0.18)	0.5118 (0.03)	0.9174 (0.03)	0.3652 (0.02)

The deposition of ZnO along the piping sections decreases as we move along the length as can be seen in Table 5. For a high mass feeding rate, the deposition is obtained until the end of the piping section, whereas for low mass feeding rate the deposition is obtained only up to the pipe-3 (P-3). This is because of the low thermophoresis gradient explained in the next section.

To see the effect of bend, air samples are drawn before and after the bend using a gross filter sampler. The mass concentration of ZnO before and after the bend for 100 and 150 $Lmin^{-1}$ experiments are measured and shown in Table 6. It can be seen that the relative loss in mass concentration is more in case of high flow rate. In high flow rate the large particles having high inertia are unable to follow the flow streamlines at bends and strike to the wall.

To obtain the aerosol mass size distribution, the aerosol-laden air was sampled by a PPASS 11-stage Cascade impactor. The sampling time varied from 2 min to 5 min depending on the concentration of generated particles. Size distributions of the sampled aerosol are summarized on a cumulative mass-weighted basis in Fig. 5 for inlet and outlet of the piping system using log-probability scaling. The Mass Mean Aerodynamic Diameter (MMAD) decreased along the length of the test assembly which can be attributed to the loss of large size particles due to impaction on the piping wall. The values of MMAD at inlet and outlet for 100 $Lmin^{-1}$ are 0.44 μm and 0.41 μm with the geometric standard deviation (GSD), 2 and 2.92, respectively (Fig. 5 (a,b)). Similarly, the values of MMAD at inlet and outlet for 150 $Lmin^{-1}$ are 0.63 μm and 0.3 μm with geometric standard deviation (GSD), 2.05 and 3.46, respectively (Fig. 5(c and d)).

The frequency size distribution of the mass concentration collected on different stages of impactor are plotted as Fig. 6 and Fig. 7 for inlet and outlet, respectively. As depicted, most of the particles are in fine ($<1\mu m$) size ranges.

4.3. Temperature profiles

During the experiment, the piping system outer wall temperature is kept at room temperature (293K). A temperature gradient gets established between the bulk gas flow and the wall of the piping which induces thermophoresis deposition. Temperature gradients are measured in all the pipe sections and plenum chamber using the thermocouples. High radial temperature gradient is observed in the plenum chamber owing to its water-cooled walls, and hence maximum thermophoretic

Table 5
Total amount of Zinc oxide deposited (in grams) on the inner sections of the piping sections.

Exp.	P-1	P-2	P-3	P-4	P-5	P-6	P-7	P-8	P-9
Exp-I(a)	0.2676	0.0543	–	–	–	–	–	–	–
Exp-I(b)	1.0786	0.5169	0.4089	0.234	0.222	0.1165	0.0942	0.1821	0.2017
Exp-II	0.1732	0.0201	0.007	–	–	–	–	–	–

Table 6
Mass concentration of Zinc oxide before and after the bend.

Experiment	Mass conc. (g/m^3) (before bend)	Mass conc. (g/m^3) (after bend)	Relative % difference
Exp-I(a)	0.68	0.55	19.11
Exp-I(b)	0.58	0.48	17.24
Exp-II	1.145	0.91	23.5

deposition is found in the diverging section of the plenum chamber as compared to other sections.

The simulated temperature of the bulk carrier gas in the piping is shown in Fig. 8. It can be seen that the agreement of the ANSYS FLUENT results with the bulk gas temperature sensors in terms of trend over the entire range of measurement locations. It was not possible to capture the accurate value of plasma flame temperature. This uncertainty in the temperature, which serves as an input to the inlet temperature for the simulation, may have caused the modeled temperature values slightly higher than the experimental values.

As mentioned earlier in Tables 4 and 5 that the deposition is higher at the inlet of the plenum chamber. This may be because of the high-temperature gradient in that region. In the experiment, the temperature gradient is not measured near the inlet region which is very close to the plasma flame and restricts the installation of temperature sensors. The temperature gradient decreases towards the outlet monotonically as can be seen in Fig. 9(a and b). The cold gas was used from the inlet which results in creating a low thermal gradient in the plenum chamber

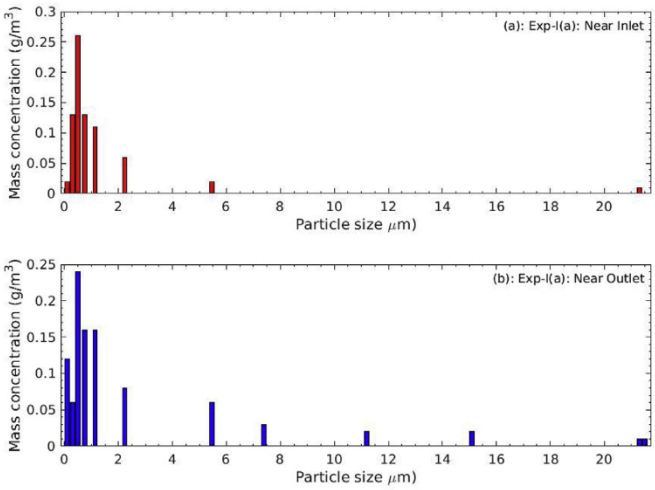

Fig. 6. Aerosol Mass size distribution for 100 $Lmin^{-1}$, (a) near inlet (b) near outlet.

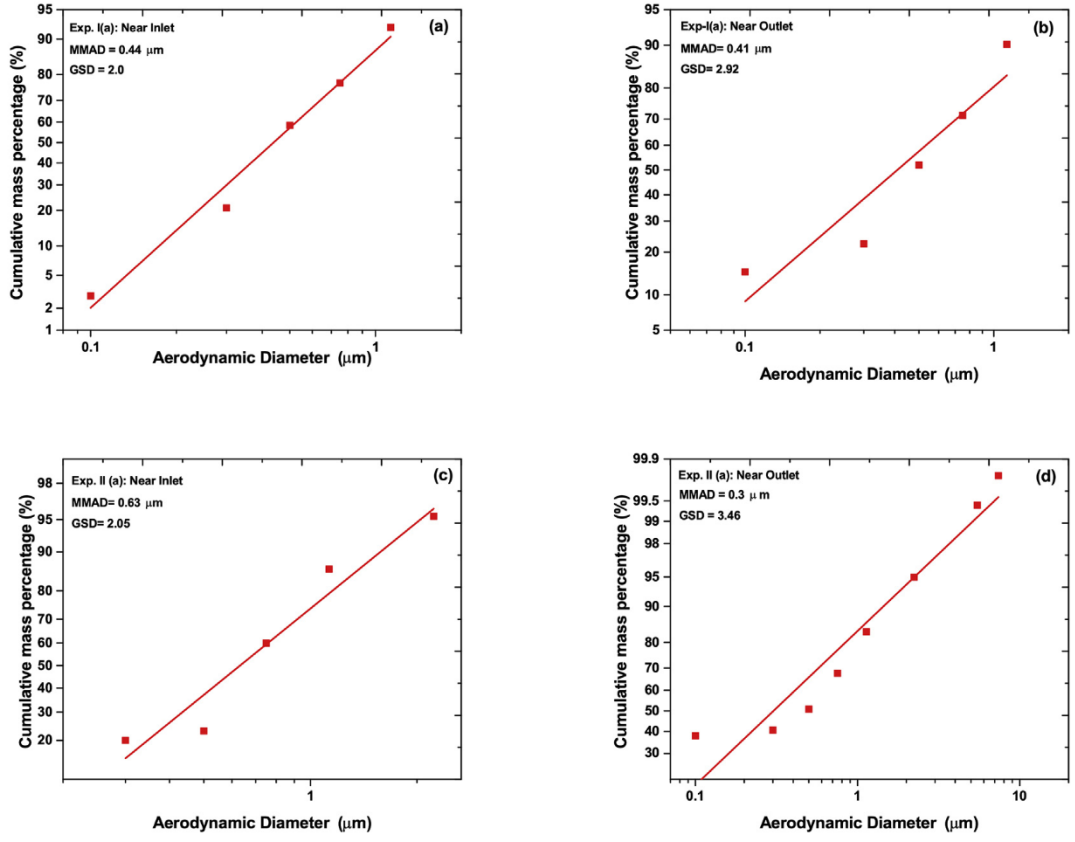

Fig. 5. Aerosol Mass size distribution for 100 $Lmin^{-1}$ (a, b) and 150 $Lmin^{-1}$ (c, d).

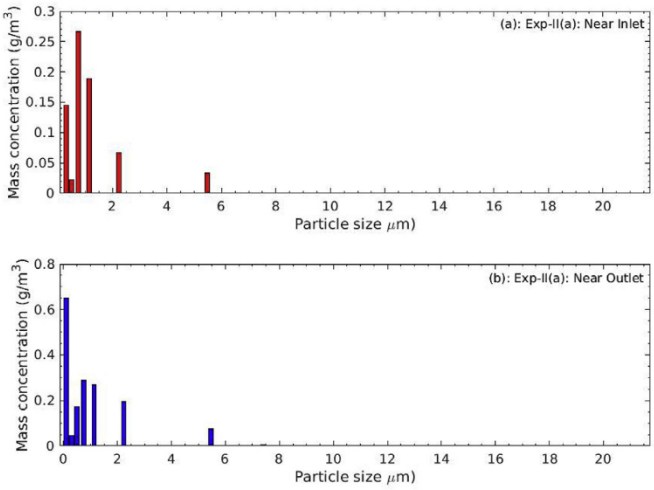

Fig. 7. Aerosol Mass size distribution for 150 $Lmin^{-1}$, (a) near inlet (b) near outlet.

(Fig. 9(a and b)).

4.4. Combined effect of thermophoresis and gravitation on PSD and mass deposition

Aerosol removal processes (i.e.dry deposition and thermophoresis) modify the number concentration and particle size distribution (PSD). In this section, the relative importance of the above mentioned aerosol removal processes is investigated. The PSD is plotted for with-and-without taking into account the deposition phenomena (dry deposition and thermophoresis) for pipe 1 at steady state. Fig. 10(a). The figure clearly shows that the injected monodispersed particles (10 nm) get coagulated, and new sizes are appear with time. It can be seen that the distribution changes significantly due to the thermophoresis and depositional effects for the small and larger sizes as compared to the intermediate particles size. Net result of these effects reflects in the behavior of total mass and number concentrations. The red curve shows the size distribution without any depositional losses. The particle size distribution in different sections in the piping system at steady state, Fig. 10(b) shows that as the particles flow through the piping sections (P1-P9), they coagulate and number concentration decreases subsequently from pipe 1 to 9.

In the plot Fig. 11 (a) the effect of gravitation and thermophoresis on the particle size number distribution for different pipe sections is presented. The curves have been normalized by respective initial particle number size distributions (i.e., distributions without any losses) to show how these effects act on the different sizes. It can be seen in Fig. 11 (a) that deposition due to gravitational and diffusional effects is dominant in the lower and the higher size ranges. The particle mass size distribution at different sections in the piping system is shown in Fig. 11 (b).

In Table 7 the mass concentrations by experiment and simulation are compared for P-1 and P-9. It can be seen that after including the depositional and thermophoretic effects the results are in good agreement.

4.5. Particle size and composition

Fig. 12, shows the X-ray diffraction pattern of the scrubbed particles from the inner wall of piping sections, contain peaks corresponding to zinc oxide.

The SEM micro graph of the deposited particles in the piping sections, Fig. 13, reveal that most of these particles are highly agglomerated, which is expected for the plasma torch–generated aerosols. The density of these agglomerated particles varies with the size; it decreases rapidly with increasing size of particle (Sapra et al., 2008). The results of the XRD and SEM analysis showed that most of the particles are in nanometer size range and consist mainly of zinc oxide.

5. Summary and conclusion

The major processes responsible for the removal of aerosol particles from the piping system and their deposition on the piping surfaces include gravitational settling and thermophoresis. These removal processes in the complex piping system are controlled to a large extent by the thermal-hydraulic conditions like temperature, pressure and flow rates. In the present work, experiments are conducted in the piping system of the National Aerosol Test Facility (NATF) with metal aerosols in dry environments with two different carrier gas flow rates. The computational fluid dynamics modeling approach is used to predict the aerosol behavior in the piping system.

Both SEM and XRD analysis on the collected samples show the samples are highly agglomerated and composed mainly of ZnO. It is found that most of the Zn particles (more than 35 %) deposit near the inlet of the plenum chamber with relatively lower deposition in subsequent piping sections. The MMAD decreases along the length of the test assembly which shows that large particles get deposited or removed in the course of flow, and only fine particles travel to the end of the piping system. The effect of bend on mass concentration is also noticed and it is found to be resulting in higher loss for the case of high flow rate. The simulation results using ANSYS Fluent match well with the experimental results of bulk gas temperature and mass concentration. It also show that the thermophoresis and depositional effects are more dominating for the small and larger sizes as compared to the intermediate particles size.

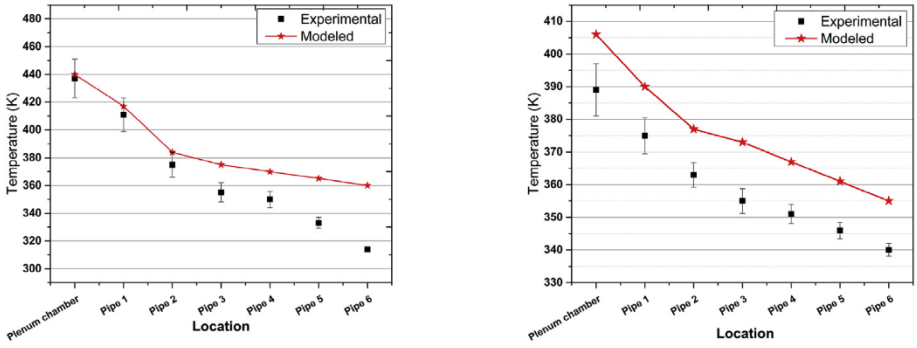

(a) 100 $Lmin^{-1}$ (b) 150 $Lmin^{-1}$

Fig. 8. Temperature at different pipe sections: Experiment and modeling.

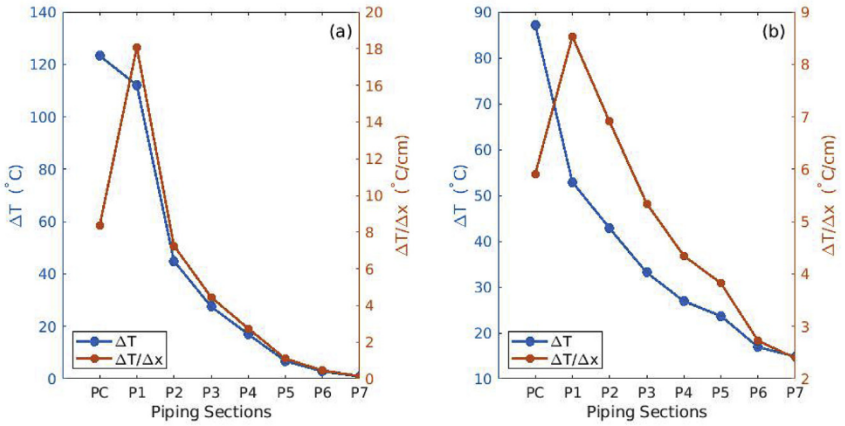

Fig. 9. Temperature gradients at different sections of the piping system: (a) 100 $Lmin^{-1}$ (b) 150 $Lmin^{-1}$.

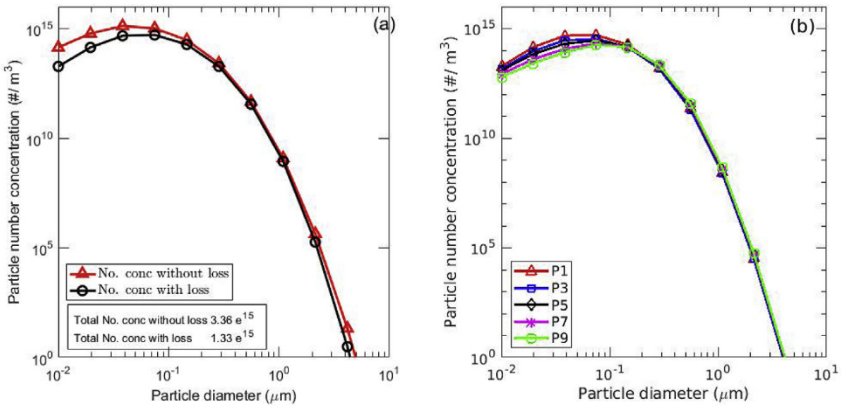

Fig. 10. (a) The effect of deposition and thermophoresis on particle size distribution, (b) The particle size distribution at different sections in the piping system at steady state. The mean size of the particles at different piping sections (P1, P3, P5, P7, P9) are 0.068 μm, 0.072 μm, 0.079 μm, 0.090 μm, 0.098 μm, respectively.

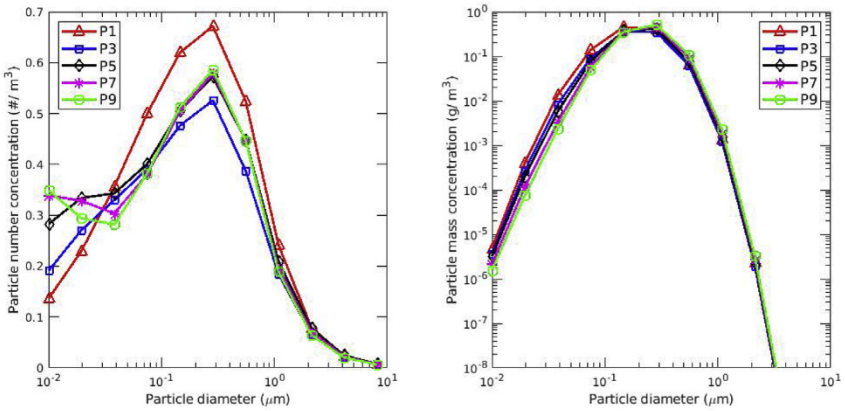

Fig. 11. (a) Normalized particle size distribution in different piping sections, (b) Mass size distribution at different sections in the piping system at steady state.

Table 7
Comparison of simulated and computed data for thermophoresis and deposition P-1 and P-9.

	P-1	P-9
Measured Mass Conc. (g/m^3)	1.10	0.91
Simulated Mass Conc. (g/m^3) (without deposition)	1.66	1.76
Simulated Mass Conc. (g/m^3) (Thermophoresis + deposition)	1.00	0.93

Acknowledgment

The present study is supported in part by Health, Safety and Environmental group, Bhabha Atomic Research Centre, Government of India. The authors also gratefully acknowledge the financial support provided by the Board of Research in Nuclear Sciences, Department of Atomic Energy, Government of India, Government of India to conduct this research under project no. 36(2,4)/15/01/2015-BRNS.

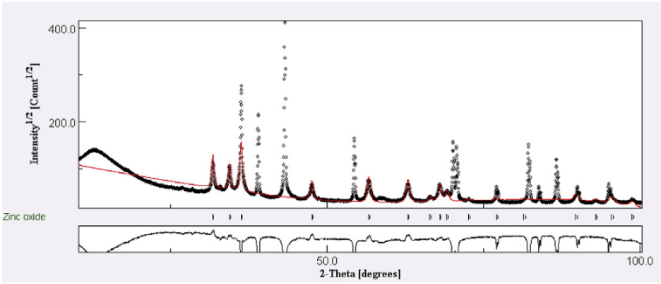

Fig. 12. XRD pattern of deposited particles.

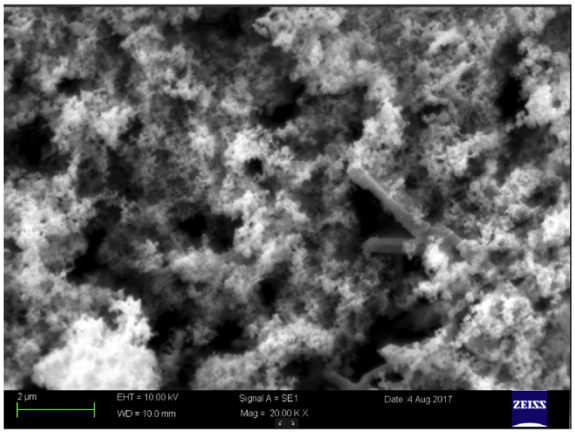

Fig. 13. SEM image of deposited particles.

Appendix A. Supplementary data

Supplementary data to this article can be found online at https://doi.org/10.1016/j.pnucene.2019.04.007.

References

Bae, B., Kim, T., Jeong, J., Kim, K., Yun, B., 2018. Droplet entrainment and deposition rates in a horizontal annular flow for space code. Prog. Nucl. Energy 109, 45–52.

Batchelor, G.K., Shen, C., 1985. Thermophoretic deposition of particles in gas flowing over cold surfaces. J. Colloid Interface Sci. 107 (1), 21–37.

Brock, J.R., 1962. On the theory of thermal forces acting on aerosol particles. J. Colloid Sci. 17 (8), 768–780.

Crump, J.G., Seinfeld, J.H., 1981. Turbulent deposition and gravitational sedimentation ofan aerosol in a vessel of arbitrary shape. Journal of Aerosol Science 12 (5), 405–415.

Firnhaber, M., Kanzleiter, T.F., Schwarz, S., Weber, G., 1996. International Standard Problem Isp37: Vanam M3-A Multi Compartment Aerosol Depletion Test with Hygroscopic Aerosol Material: Comparison Report. Organisation for Economic Co-Operation and Development-Nuclear Energy Agency Technical report.

Gelbard, F., Seinfeld, J.H., 1979. The general dynamic equation for aerosols. theory and application to aerosol formation and growth. J. Colloid Interface Sci. 68 (2), 363–382.

Ghosh, K., Tripathi, S.N., Joshi, M., Mayya, Y.S., Khan, A., Sapra, B.K., 2017. Modeling studies on coagulation of charged particles and comparison with experiments. J. Aerosol Sci. 105, 35–47.

Jokiniemi, J., Auvinen, A., Mäkynen, J., Valmari, T., Energy, V., 1998. Fission Product Behaviour in Severe Accidents. The Finnish Research Programme on Reactor Safety, pp. 145.

Joshi, S.V., Liang, Q., Park, J.Y., Batdorf, J.A., 1990. Effect of quenching conditions on particle formation and growth in thermal plasma synthesis of fine powders. Plasma Chem. Plasma Process. 10 (2), 339–358.

Le Marois, G., Megnin, M., 1994. Assessment of fission product deposits in the reactor coolant system: the devap program. Nucl. Saf. 35 (2), 213–221.

Liu, B.Y.H., Agarwal, J.K., 1974. Experimental observation of aerosol deposition in turbulent flow. J. Aerosol Sci. 5 (2), 145–155.

Longest, P.W., Xi, J., 2007. Effectiveness of direct Lagrangian tracking models for simulating nanoparticle deposition in the upper airways. Aerosol Sci. Technol. 41 (4), 380–397.

Maruyama, Y., Shibazaki, H., Igarashi, M., Maeda, A., Harada, Y., Hidaka, A., Sugimoto, J., Hashimoto, K., Nakamura, N., 1999a. Vapor condensation and thermophoretic aerosol deposition of cesium iodide in horizontal thermal gradient pipes. J. Nucl. Sci. Technol. 36 (5), 433–442.

Maruyama, Y., Shibazaki, H., Igarashi, M., Maeda, A., Harada, Y., Hidaka, A., Sugimoto, J., Hashimoto, K., Nakamura, N., 1999b. Vapor condensation and thermophoretic aerosol deposition of cesium iodide in horizontal thermal gradient pipes. J. Nucl. Sci. Technol. 36 (5), 433–442.

Mishra, G., Mandariya, A.K., Tripathi, S., Joshi, M., Khan, A., Sapra, B., et al., June 2019. Hygroscopic growth of csi and csoh particles in context of nuclear reactor accident research. J. Aerosol Sci. 132, 60–69.

Modi, R., Khan, A., Joshi, M., Ganju, S., Singh, A.K., Srivastava, A., Sapra, B.K., Mayya, Y.S., 2014. Metal oxide aerosol dry deposition in laminar pipe flow at high thermal gradients and comparison with sophaeros module of astec reactor accident analysis code. Ann. Nucl. Energy 64, 107–113.

Parker, S., Foat, T., Preston, S., 2008. Towards quantitative prediction of aerosol deposition from turbulent flows. J. Aerosol Sci. 39 (2), 99–112.

Šadek, S., Grgić, D., Šimić, Z., 2017. Application of Astec, Melcor, and Maap Computer Codes for Thermal Hydraulic Analysis of a Pwr Containment Equipped with the Pcfv and Par Systems. Science and Technology of Nuclear Installations 2017.

Sapra, B.K., Mayya, Y.S., Khan, A., Sunny, F., Ganju, S., Kushwaha, H.S., 2008. Aerosol studies in a nuclear aerosol test facility under different turbulence conditions. Nucl. Technol. 163 (2), 228–244.

Seinfeld, H.J., Pandis, N.S., 1998. Atmospheric Chemistry and Physics, from Air Pollution to Climate Change. John Wiley, New York.

Sher, R., Hobbins, R.R., 2011. Transport and Removal of Aerosols in Nuclear Power Plants Following Severe Accidents. American Nuclear Society.

Sher, R., Hoover, M.D., Newton, G.J., Rahn, F.J., 1994. Aerosol behavior in nuclear facilities. Trans. Am. Nucl. Soc. 70 CONF-940602–.

Shimada, M., Okuyama, K., Kousaka, Y., 1989. Influence of particle inertia on aerosol deposition in a stirred turbulent flow field. J. Aerosol Sci. 20 (4), 419–429.

Shimada, M., Seto, T., Okuyama, K., 1994. Wall deposition of ultrafine aerosol particles by thermophoresis in nonisothermal laminar pipe flow of different carrier gas. Jpn. J. Appl. Phys. 33 (2R), 1174.

Singh, S., Khan, A., Das, T., Sapra, B.K., Pushparaja, Mayya, Y.S., 2005. Indigenous Development of an Aerodynamic Size Separator for Aerosol Size Distribution Studies. Current Science, pp. 1426–1433.

Sreekumar, K., 1996. Plasma Torch Based Aerosol Generator. Bhabha Atomic Research Centre B.A.R.C. (Series).

Stratmann, F., Fissan, H., 1989. Experimental and theoretical study of submicron particle transport in cooled laminar tube flow due to combined convection, diffusion, and thermophoresis. J. Aerosol Sci. 20 (8), 899–902.

Talbot, L., Cheng, R.K., Schefer, R.W., Willis, D.R., 1980. Thermophoresis of particles in a heated boundary layer. J. Fluid Mech. 101 (4), 737–758.

Vohra, K., Ghosh, K., Tripathi, S.N., Thangamani, I., Goyal, P., Dutta, A., Verma, V., 2017. Submicron particle dynamics for different surfaces under quiescent and turbulent conditions. Atmos. Environ. 152, 330–344.

Waldmann, L., Schmitt, K.H., 1966. Thermophoresis and Diffusiophoresis of Aerosols. Academic Press, New York.

Walker, K.L., Homsy, G.M., Geyling, F.T., 1979. Thermophoretic deposition of small particles in laminar tube flow. J. Colloid Interface Sci. 69 (1), 138–147.

Williams, M., 1990. Nuclear aerosol behavior during reactor accidents. Prog. Nucl. Energy 23 (2), 101–108.